

Spin-phonon dispersion in magnetic materials

Mingqiang Gu

*Department of Physics, Southern University of
Science and Technology, Shenzhen 518055, China*

Y. H. Bai

*Office of Information Technology, Indiana State
University, Terre Haute, Indiana 47809, USA*

G. P. Zhang*

Department of Physics, Indiana State University, Terre Haute, Indiana 47809, USA

Thomas F. George

*Departments of Chemistry & Biochemistry and Physics & Astronomy,
University of Missouri-St. Louis, St. Louis, MO 63121, USA*

(Dated: July 22, 2022)

Abstract

Microscopic coupling between the electron spin and the lattice vibration is responsible for an array of exotic properties from morphic effects in simple magnets to magnetodielectric coupling in multiferroic spinels and hematites. Traditionally, a single spin-phonon coupling constant is used to characterize how effectively the lattice can affect the spin, but it is hardly enough to capture novel electromagnetic behaviors to the full extent. Here, we introduce a concept of spin-phonon dispersion to project the spin moment change along the phonon crystal momentum direction, so the entire spin change can be mapped out. Different from the phonon dispersion, the spin-phonon dispersion has both positive and negative frequency branches even in the equilibrium ground state, which correspond to the spin enhancement and spin reduction, respectively. Our study of bcc Fe and hcp Co reveals that the spin force matrix, that is, the second-order spatial derivative of spin moment, is similar to the vibrational force matrix, but its diagonal elements are smaller than the off-diagonal ones. This leads to the distinctive spin-phonon dispersion. The concept of spin-phonon dispersion expands the traditional Elliott-Yafet theory in nonmagnetic materials to the entire Brillouin zone in magnetic materials, thus opening the door to excited states in systems such as CoF_2 and NiO , where a strong spin-lattice coupling is detected in the THz regime.

PACS numbers: 75.40.Gb, 78.20.Ls, 75.70.-i, 78.47.J-

Keywords: Spin, phonon, magnetism, dispersion, force matrix, Elliot-Yafet theory

I. INTRODUCTION

Using the lattice to control the spin degree of freedom has garnered a significant attention worldwide, as a new way to alter spintronics. But long before the current surging research activities [1–3], phonon excitation is known to be essential to demagnetization in a magnetic material by transferring energy to the spin subsystem, inducing magnetic phase transition. Even in nonmagnetic crystals, the magnetic field affects photon-phonon interactions, which is known as morphic effects [4]. The discovery of strong magnetodielectric coupling in Mn_3O_4 [5] demonstrated that the lattice involvement is more than just energy transfer. Hirai *et al.* [6] reported a large atomic displacement at a magnetic phase transition, with structural change detected [7]. Extreme modification on the crystal lattice is expected to change the magnetic ordering and has been demonstrated experimentally with multiferroic $(\text{La,Ca})\text{MnO}_3$ [8]. The Raman scattering experiment [9] revealed that there is an opposite effect on the lattice from an external magnetic field, or magnetostructure change. A real-space magnetic imaging of multiferroic spinel was also obtained experimentally [10]. When lattice vibrates, it alters the exchange interaction [11]. Theoretically, Lizarraga *et al.* [12] showed the magnetism itself may play a role in the phase transition from hcp Co to fcc Co. Kuang *et al.* [13] suggested that Co may have magneto-elastic effects. Verstraete [14] showed that the electron-phonon coupling is also spin-dependent and the spin minority band has a larger coupling than the majority one. Lefkidis *et al.* [15] demonstrated for the first time that the phononic effects also appear on an ultrashort time scale, through the electron-phonon coupling [16, 17]. The effect becomes stronger in the rare-earth $\text{Gd}(0001)$ [18, 19]. Henighan *et al.* [20] directly detected the signature of THz coherent acoustic phonons in Fe. To characterize the coupling between the phonon and spin excitation, a common method is to use the phonon-magnon coupling or magnetoelastic coupling [21–28]. Pattanayak *et al.* [29] recently detected some of the key signatures of spin-phonon coupling in hematite crystallites through dielectric and Raman spectroscopy. However, a single spin-phonon coupling constant is hardly enough to capture the complexity as how spin and phonon interact with each other. The lattice vibration has $3N - 6$ degrees of freedom for a system of N atoms, which is likely to limit the scope of applications of a single spin-phonon coupling constant, especially true in magnetostructure and magnetodielectric coupling.

In this paper, we go beyond a single spin-phonon coupling constant and introduce a

concept of the spin-phonon dispersion. We take the hcp Co as our first example to show that there is a well-defined nearly linear dependence of the spin moment on the volume of the cell for a fixed c/a ratio, and on the c/a ratio for a fixed volume. The second order in the spin moment change is dispersed along the phonon crystal momentum. A new picture emerges. Different from the phonon counterpart, the eigenvalues of the spin-phonon dispersion can be either positive or negative, which corresponds to the spin moment increase or decrease, respectively. The orders of the spin-phonon bands are reversed with respect to the phonon dispersion; and at the Γ point the single-degenerate band appears at the bottom and the triple-degenerate band at the top. Along the high symmetry lines in the Brillouin zone, both spin reduction and enhancement are found. The situation in bcc Fe is different. The major reduction is around the N point, and there is only spin enhancement along the Γ -H line. We attribute the main differences between the spin-phonon dispersion and the regular phonon dispersion to their respective force matrices. While the matrix for second derivative of spin with respect to atomic displacement, i.e., the spin force matrix, has a similar structure as the vibrational force matrix, its diagonal elements are smaller than its off-diagonal elements, so the spin dynamical matrix has both negative and positive eigenvalues. The spin-phonon dispersion proposed here is expected to be applicable across all magnetic materials; it points out regions where the spin properties can be tailored through the phonon excitation.

The rest of the paper is arranged as follows. In Sec. II, we present the theoretical formalism, where we first define the spin dynamical matrix and then present the details of the spin-phonon dispersion calculation. Section III provides our results, where the spin change in hcp Co for two phonon modes is first examined, followed by the spin-phonon dispersions of hcp Co and bcc Fe. We explain these main differences using the vibrational force and spin force matrices. Section IV is devoted to the discussion of our results and their relation to the ongoing experimental research and the Elliot-Yafet theory. We conclude this paper in Sec. V.

II. THEORETICAL FORMALISM

Even in nonmagnetic metals, the traditional Elliot-Yafet (EY) theory [30, 31] has shown that phonons play a significant role in spin relaxation. Spin hot spots were identified in polyvalent metals [32, 33]. In magnetic materials, states are spin-polarized and with the

presence of spin-orbit coupling, one has to introduce the SD factor to characterize the spin hot spots in laser-induced demagnetization [34], which highlights the fact that a single spin-phonon coupling parameter is not enough.

Here we employ the density functional theory as implemented in the Wien2k code [35] and VASP code [36], with the details presented elsewhere [37–41]. In brief, we solve the Kohn-Sham equation self-consistently [40],

$$\left[-\frac{\hbar^2 \nabla^2}{2m_e} + v_{eff}(\mathbf{r}) \right] \psi_{i\mathbf{k}}(\mathbf{r}) = E_{i\mathbf{k}} \psi_{i\mathbf{k}}(\mathbf{r}), \quad (1)$$

where $\psi_{i\mathbf{k}}(\mathbf{r})$ and $E_{i\mathbf{k}}$ are the eigenstate and eigenenergy of band i and \mathbf{k} point, respectively. v_{eff} is determined by

$$v_{eff}(\mathbf{r}) = v(\mathbf{r}) + \int \frac{n(\mathbf{r}')}{|\mathbf{r} - \mathbf{r}'|} d\mathbf{r}' + v_{xc}(\mathbf{r}), \quad (2)$$

where $v_{xc}(\mathbf{r})$ is the exchange-correlation potential, $v_{xc}(\mathbf{r}) = \delta E_{xc}[n]/\delta n(\mathbf{r})$. The spin-orbit coupling is included through the second variational principle [35]. We use the generalized gradient approximation for the exchange-correlation energy functional. The density $n(\mathbf{r})$ is computed from $n(\mathbf{r}) = \sum_{i\mathbf{k}} \rho_{i,i,\mathbf{k}} |\psi_{i\mathbf{k}}(\mathbf{r})|^2$, where $\rho_{i,i,\mathbf{k}}$ is the electron occupation.

The lattice dynamics is governed by the potential energy change around the equilibrium position of lattice points. The expansion of the potential energy Φ is

$$\Phi(\mathbf{R}) = \Phi_0 + \sum_{i,\alpha} \left(\frac{\partial \Phi}{\partial R_{i,\alpha}} \right)_0 \Delta R_{i,\alpha} + \frac{1}{2} \sum_{i,\alpha;j,\beta} \left(\frac{\partial^2 \Phi}{\partial R_{i,\alpha} \partial R_{j,\beta}} \right)_0 \Delta R_{i,\alpha} \Delta R_{j,\beta} + \dots \quad (3)$$

where $R_{i,\alpha}$ denotes the position of atom i along the α direction. At equilibrium, the second term is zero because the net forces on all atoms should be zero. So the lowest order in the potential is the second order (the third term in the equation). The second-order potential derivative matrix \mathcal{P} , the vibration force matrix, is defined as

$$\mathcal{P}_{ij}^{\alpha\beta} = \left(\frac{\partial^2 \Phi(\mathbf{L}_i - \mathbf{L}_j)}{\partial R_{i,\alpha} \partial R_{j,\beta}} \right)_0, \quad (4)$$

which is used to compute the phonon spectrum. Here \mathbf{L}_i and \mathbf{L}_j are the lattice vectors for atoms i and j , respectively. Terms higher than the second order are ignored.

Similar to the lattice vibration, the total magnetic spin moment of a crystal can be expanded as a function of the displacements of the atoms, i.e.,

$$M_s = M_0 + \sum_{i,\alpha} \left(\frac{\partial M_s}{\partial R_{i,\alpha}} \right)_0 \Delta R_{i,\alpha} + \frac{1}{2} \sum_{ij,\alpha\beta} \left(\frac{\partial^2 M_s}{\partial R_{i,\alpha} \partial R_{j,\beta}} \right)_0 \Delta R_{i,\alpha} \Delta R_{j,\beta} + \dots, \quad (5)$$

where M_s is the magnetic moment of the crystal, M_0 is the magnetic moment at the lattice equilibrium, \mathbf{R} is the position of the atom, $i(j)$ is the atomic index, and $\alpha(\beta)$ is the direction index, i.e., $\alpha = x, y,$ or z . Different from the phonon calculation above, the linear term (the second term) $\left(\frac{\partial M_s}{\partial R_{i,\alpha}}\right)_0$ is not zero, because the energy minimum is not the spin moment minimum in a magnetic material. The second-order derivative of the spin moment \mathcal{S} , spin force matrix, is defined similarly as,

$$\mathcal{S}_{ij}^{\alpha\beta}(\mathbf{L}_i - \mathbf{L}_j) = \left(\frac{\partial^2 M_s(\mathbf{L}_i - \mathbf{L}_j)}{\partial R_{i,\alpha} \partial R_{j,\beta}}\right)_0, \quad (6)$$

which only depends on the relative lattice vector \mathbf{L} . In this work, we use the finite difference method in a $(2 \times 2 \times 2)$ supercell to find the second order spin moment change. Figure 1 shows a two-cell structure for bcc Fe, where the first nearest neighbor and the second nearest neighbor atoms are denoted by the dashed and dotted lines, respectively. The spin dynamical matrix is

$$\mathcal{C}_{ij}^{\alpha\beta}(\mathbf{k}) = \sum_{\mathbf{L}} \mathcal{S}_{ij}^{\alpha\beta}(\mathbf{L}) e^{-i\mathbf{k}\cdot\mathbf{L}}, \quad (7)$$

where \mathbf{k} is the reciprocal lattice vector. We diagonalize it to get the spin-phonon dispersion spectrum. The first order change in spin moment, which is already taken into account in the EY theory [30, 31], only contributes a shift in the displacement, so it is not included under our current theory.

III. RESULTS

Despite the apparent importance of spin-lattice interaction in many materials [42, 43], except a short presentation [44], there has been no prior study on how the spin moment changes with the lattice. Our study is also different from prior studies on magnon-phonon coupling [21] where the spin wave, i.e. the spatial orientation of the spins, at each lattice site is coupled to the vibration but the spin amplitude remains the same. Here, we consider the spin amplitude change when the atoms vibrate. For this reason, it is necessary to develop a simple picture before the full scale of calculation.

A. Effects of breathing and stretching modes on the spin moment in hcp Co

We strategically choose hcp Co as our first example, because without changing the unit cell size we can already investigate two vibrational modes: one is the breathing mode, where

the volume is changed while keeping the ratio c/a fixed, and the other is the stretching mode, where the ratio c/a is changed by keeping V fixed. Our in-plane lattice constant a is 4.713924 bohr, and out-of-the-plane one c is 7.651595 bohr. The unit cell volume is $V = \sqrt{3}a^2c/2$ [45]. Here we use the Wien2k code to carry out our study. We choose the Muffin-tin radius R_{MT} of 2.26 bohr, and its product with the planewave cutoff K_{cutoff} is 9. The k mesh is $33 \times 33 \times 17$, which is sufficient to converge our results as tested before [45].

Figure 2(a) shows the total energy change $\Delta E = E - E_{\text{min}}$ as a function of volume change $\Delta V/V$ for the breathing mode, where E_{min} is the energy minimum. We see that the entire change is very smooth and forms a typical parabola with a minimum around -0.2%, which shows that our starting lattice constant is slightly too large, but this does not affect our conclusion. By contrast, the spin moment (M_S) change increases linearly with $\Delta V/V$ (see Fig. 2(b)). For every 1% change in $\Delta V/V$, the spin changes by about $0.01 \mu_B$, which can be fitted to $M_S = [1.73 + 0.00965\Delta V/V - 0.0001469(\Delta V/V)^2] \mu_B$, where the second term is the linear contribution. Figure 2(c) shows the orbital moment change with $\Delta V/V$, which can be fitted to $M_O = (0.0778 + 0.00189\Delta V/V)\mu_B$. The orbital change is only 1/5 the spin change. The results from the stretching mode are shown in Figs. 2(d), (e), and (f). Figure 2(d) shows that the stretching mode has a similar smooth energy change as a function of c/a . Its spin change (Fig. 2(e)) is smaller than that in the volume change; and for one percentile change in c/a , the spin changes by $0.001895 \mu_B$. The second order coefficient is below 10^{-6} . The orbital M_O behaves very differently from the spin: it decreases with c/a (Fig. 2(f)), and the change is not strictly linear. So far the spin changes are limited to two lattice modulations. To go beyond this, we need to introduce the spin-phonon dispersion.

B. Spin-phonon dispersion

We start with hcp-Co. There have been many studies on the phonon dispersion of hcp Co. For instance, Pun and Mishin *et al.* [46] employed the embedded-atom potential to compute the phonon spectrum. We employ the VASP code [36] and the frozen-phonon method and our computed phonon dispersion is shown in Fig. 3(a). The frequencies of the two optical modes at Γ point are 4.45 (doublet) and 7.12 (singlet) THz, respectively, which match the neutron scattering results [47] of 4.30 and 7.60 THz, respectively. This agreement gives us confidence that our theory can give an accurate prediction on the lattice dynamics.

We then move on to the spin moment change as a function of lattice vibration. As predicted by Eq. 5, the spin has a nonzero second-order term in the lattice displacement. We make the same Born-Oppenheimer approximation for the spin where the lattice responds much slower than the electron spin, an assumption that needs experimental verification. Then we can apply the same frozen-phonon method to the spin moment change as a function of atomic displacement. By diagonalizing the spin dynamical matrix (Eq. 7), we obtain the spin dispersion as a function of the crystal momentum. Physically, this represents the spin moment change as the atoms vibrate according to the normal modes of phonons.

Figure 3(b) is our spin dispersion for hcp Co. The high symmetry points are highlighted with the dashed vertical lines. The general structure follows the phonon (Fig. 3(a)), but the order of the spectrum is different. At the Γ point, the phonon spectrum has three acoustic bands at the bottom but the spin has them at the top. In addition, the degeneracy increases from 1 to 3 from the bottom to the top. The horizontal line sets the zero value for the spin dispersion. This feature persists from Γ to K, but at the M point, similar to the phonon spectrum, no degeneracy is found. At the A point, all the bands are close to a single point.

The major difference from the phonon spectrum is that the spin dispersion has several branches with “imaginary modes” (negative eigenvalues). Just as the imaginary phonon modes leading to the structural instability, the spin imaginary modes lead to spin reduction or demagnetization. The activation of those modes reduce the magnitude of the total spin moment. This phonon-induced demagnetization process is different from the conventional magnon picture or thermal-based demagnetization mechanism where the spin spatial orientation change reduces the spin moment for the entire sample. In our case, the magnitude of the local spin moment is changed as the atom vibrates along the eigenvector of a phonon mode. Quantitatively, if we examine Fig. 3(b) closely, we notice that the LO mode at the Γ point has a larger contribution to the reduction of spin moment than that of the two fold degenerate TO modes. The reason why these modes behave differently can be explained by examining the Co-Co bond. Physically, the longitudinal mode shortens the bond length on one side, while elongates it on the other. When the distance between neighboring atoms decreases, the increased electron overlap broadens the 3d bandwidth and reduces the density of state at the Fermi level. This mechanism is also the origin of the suppression of the magnetization when the lattice constant of Co reduces. By contrast, the transverse mode acts differently. Instead of changing the bond length, it distorts the angles between lattice

vectors, i.e. changing the bond angles. In other parts of the Brillouin zone, both the spin increase and decrease are found. This is our first major finding.

This spin moment change is not limited to hcp Co. In bcc Fe, we find a similar pattern. Figure 3(c) is our phonon dispersion. With fewer atoms in the cell, the number of bands is reduced. Our spin-phonon dispersion is shown in Fig. 3(d). Between the Γ and H points, the spin-phonon and the phonon dispersions are almost identical, but the major difference appears around the N point, where we see a major negative eigenvalue branch. This corresponds to the spin moment reduction. However, the spin enhancement dominates along these high symmetry lines. The k -point convergence test has been performed up to $(32 \times 32 \times 32)$. The data in the paper uses the k -point mesh of $(16 \times 16 \times 16)$.

C. Insights into the spin-phonon dispersion

To have a deeper understanding of the phonon-induced spin moment change, we compare the vibrational force matrix $\mathcal{P}_{ij}^{\alpha\beta}$ and the spin force matrix $\mathcal{S}_{ij}^{\alpha\beta}$, where i and j are the atom indices and $\alpha\beta$ are the Cartesian coordinate indices. These two matrices are used to compute the phonon and spin-phonon dispersions. We take bcc Fe as an example. For the supercell $2 \times 2 \times 2$, eight atoms are at positions, $(0, 0, 0)$, $(\frac{1}{2}, \frac{1}{2}, 0)$, $(\frac{1}{2}, 0, \frac{1}{2})$, $(0, \frac{1}{2}, \frac{1}{2})$, $(\frac{1}{2}, 0, 0)$, $(0, \frac{1}{2}, 0)$, $(0, 0, \frac{1}{2})$, $(\frac{1}{2}, \frac{1}{2}, \frac{1}{2})$. So there are 64 combinations, leading to sixty-four 3×3 matrices along the x , y and z axes. The simplest matrix is the on-site one.

$$\mathcal{S}_{1,1} = \begin{pmatrix} \gamma & 0 & 0 \\ 0 & \gamma & 0 \\ 0 & 0 & \gamma \end{pmatrix}; \quad \mathcal{P}_{1,1} = \begin{pmatrix} g & 0 & 0 \\ 0 & g & 0 \\ 0 & 0 & g \end{pmatrix}. \quad (8)$$

It is clear that the spin and vibrational force matrices have the same structure. This is true for four matrices for the nearest neighbors in the same primitive cell,

$$\mathcal{S}_{1,5} = \begin{pmatrix} -\alpha & \beta & \beta \\ \beta & -\alpha & -\beta \\ \beta & -\beta & -\alpha \end{pmatrix}; \quad \mathcal{P}_{1,5} = \begin{pmatrix} -a & b & b \\ b & -a & -b \\ b & -b & -a \end{pmatrix}, \quad (9)$$

but we notice a crucial difference. In the spin force matrix, the diagonal element α is always smaller than the off-diagonal element β , where α and β are matrix elements, not to be confused with the direction indices above. Numerically, if we use those $\mathcal{S}_{1,5}$ matrices alone,

we end up to have a negative eigenvalue. This explains why the spin-phonon dispersion has a negative eigenvalue, but the phonon one does not. The other three matrices are found by cyclically exchanging the off-diagonal elements.

Another major difference is in the matrices for the next nearest neighbor cell.

$$\mathcal{S}_{1,2} = \begin{pmatrix} \delta & 0 & 0 \\ 0 & \delta & 0 \\ 0 & 0 & \epsilon \end{pmatrix}; \quad \mathcal{P}_{1,2} = \begin{pmatrix} -d & 0 & 0 \\ 0 & -d & 0 \\ 0 & 0 & -e \end{pmatrix}. \quad (10)$$

The other two matrices can be reproduced by the cyclic relation. One sees that the spin force matrix has a positive value, but the vibrational force matrix is all negative. Since both the vibrational force matrix and the spin force matrix must obey the sum rule, where the summation over the cells and atoms is zero, we find that for the spin, $\gamma + 2\delta + 1\epsilon - 4\alpha = 0$, but for the vibration, $g - 2d - 1e - 4a = 0$. All the parameters are given in Table I.

IV. DISCUSSIONS AND IMPLICATION FOR EXPERIMENTS

In nonmagnetic metals, the spin lifetime τ_s is equal to the electron momentum relaxation time multiplied by the EY constant β , which is the ratio of the energy gap ΔE to the spin-orbit coupling λ_{soc} [30, 31]:

$$\tau_s = \beta\tau_e = \left(\frac{\Delta E}{\lambda_{soc}}\right)^2 \tau_e \quad (11)$$

where the energy gap ΔE is between two scattering states. For multiple channels of scattering, the inverse spin lifetime $1/\tau_s$, or the rate of spin relaxation, is computed from

$$\frac{1}{\tau_s} = \sum_i \frac{1}{\beta_i\tau_{e,i}}. \quad (12)$$

This relation is controlled by the smallest β_i , which is often the phonon, β_{phonon} . Fabian and Das Sarma [32] further showed in polyvalent metals, such as Al, that the spin relaxation is significantly increased around spin hot spots [33], where a Fermi surface cuts through the Brillouin zone boundaries and special symmetry points and lines. Experiments showed that β is not even a constant and depends on surfaces and interfaces [48]. In magnetic materials, this is much more complicated [34] and also more important for spintronics.

Here, we make a moderate attempt to show that the lattice distortion affects the spin and spin flip among the band states, with a detailed study left for the future due to the enormous

complications in magnetic materials. We choose two states close to the Fermi level, band states 38 and 39. Due to the band dispersion, we cannot guarantee that they always stay close to the Fermi level. All the conclusions drawn here are specific to these two states, and should not be applied to others without a detailed calculation. Initially, we aim to choose a special symmetry line, from Γ to A, along the k_z axis, but it turns out that due to the momentum locking in the spin-orbit coupling, along this direction there is almost no spin flip. Since showing results for a k mesh of $(53 \times 53 \times 28)$ is overly excessive, we decide to choose five segments which are not along any high symmetry lines. The k only changes along the z axis from 0 to 0.5 in the units of the reciprocal lattice vector, so we can monitor the pattern of change. Other than this, the k choice is arbitrary. Segment 1, from 361 to 375, has the k change from $k_0 = (0, 0.45, 0)$ to $k_1 = (0, 0.45, 0.5)$, where the numbers 361 to 375, as well as those on the x axis of Fig. 4, are the k index of the k list out of $(53 \times 53 \times 28)$. Segment 2, from 376 to 390, has the k change from $(0, 0.4716, 0)$ to $k_2 = (0, 0.4716, 0.5)$; segment 3, from 391 to 405, has the k change from $(0, 0.4905, 0)$ to $k_3 = (0, 0.4905, 0.5)$; segment 4, from 406 to 420, has the k change from $(0, 0.01886, 0)$ to $k_4 = (0, 0.01886, 0.5)$; and segment 5, from 421 to 435, has the k change from $(0.001886, 0.0377, 0)$ to $k_5 = (0.001886, 0.0377, 0.5)$.

Figures 4(a) and (b) show the spin moments $\langle nk|s_z|nk\rangle$ of states 38 and 39 and the spin flipping $\langle nk|s^+|mk\rangle$ and $\langle nk|s^-|mk\rangle$ between them, where s_z is the z -component of the spin operator, and s^\pm are the raising and lowering spin operators, respectively. Figure 4(a) reveals that most of the k points have spin moment close to either $+1\mu_B$ or $-1\mu_B$. These spin moments are not exactly at $+1\mu_B$ or $-1\mu_B$; with the spin-orbit coupling, either $+1\mu_B$ or $-1\mu_B$ is not allowed for states with a nonzero orbital angular momentum. In the first segment between k_0 and k_1 , state 38 has spin moment close to $-1\mu_B$, and state 39 has spin moment close to $+1\mu_B$, but this is not enough to have a spin flip. Figure 4(b) shows that the spin flip between them is small because the spin flip, the expectation value of $\langle 38|s^+|39\rangle$, critically depends on the product of the small spin component of one state's wavefunction with the large spin component of another state. $\langle 38|s^-|39\rangle$ is not shown since it is very small for this pair of states. The first maximum occurs at the end of the first segment k_2 , where the spin of state 28 drops to $-0.69\mu_B$. A smaller spin flip is at k_3 and k_4 . If we slightly distort the lattice in the same fashion as Figs. 2(d), (e) and (f) (the lattice change is -5%), we can investigate the effect of the lattice vibration. Figure 4(c) shows that while the majority of the spins remain similar to Fig. 4(a), the hot spin pockets [34] are relocated

to different k points. A bigger change is in the spin flip, with the maximum shifted to k_3 . This shows that the spin flipping is very sensitive to the lattice perturbation. Numerically we find that the initial wavefunctions that form the basis of the spin-orbit coupling in the second-variational step have a significant impact on the phase of the matrix elements of s^+ and s^- , but the effect on the s_z is tiny. Our results may change if the wavefunction is converged at a different criterion. In our calculation, we use an extremely low charge convergence of 10^{-7} . We should point out that Fig. 4 only samples a small portion of the Brillouin zone and one should not conclude that the distorted structure has a smaller spin flip, since a significant variation of the spin flip in comparison to the undistorted structure is found across the entire Brillouin zone. Our goal here is to show that the phonons do affect the spin flip, highlighting the importance of the spin-phonon dispersion.

The negative eigenvalues found in the spin-phonon dispersion identify a demagnetization channel through the nearest neighbor vibration, which could have some implications on the recent debate on the mechanism of femtomagnetism [49–51]. It has been argued that the phonon plays a significant role in demagnetization [52, 53]. While we do not consider the electronic excited state, the spin-phonon dispersion demonstrates unambiguously that not every phonon excitation leads to demagnetization. If we assume a harmonic oscillation of lattice with time as shown by Henighan *et al.* [20], we expect that the spin oscillates as $M_S(t) = M_S^{(0)} + M_S^{(1)} \sin(\Omega t)$, where t is the time, $M_S^{(0)}$ and $M_S^{(1)}$ are two constants, and Ω is the phonon frequency. This does not necessarily correspond to demagnetization. In hcp Co, Fig. 3(b) shows that the maximum negative eigenvalue reaches $-3.7 \mu_B/\text{\AA}^2$ at Γ , which corresponds to the optical phonon mode in Fig. 3(a). If we suppose the phonon mode displacement to be 0.01\AA , which is typical in solids, this leads to the spin moment reduction of $-3.7 \times 10^{-4} \mu_B$, which is quite small. However, there are at least two cases that the spin reduction can be boosted. One is the multiphonon generation which is featured by the THz anharmonic frequency shift [54, 55]. Under the same temperature, lower-frequency phonon modes are generated more. At an elevated temperature, we expect that the lattice vibration anharmonicity appears since the coupling between the phonon and demagnetization becomes highly nonlinear. This may contribute additional amounts of demagnetization. The second case is if one employs a strong laser pulse, where the displacement can reach 0.5\AA . In bcc Fe, even though only one pocket has a larger negative eigenvalue (around N), its value, $-4.4 \mu_B/\text{\AA}^2$, is more negative than that in hcp Co. This suggests a scenario for future experiments.

If one can selectively excite a special phonon mode, through Raman or neutron scattering [56], and then detect the spin moment change, one may be able to completely map out the entire spin-phonon dispersion.

Finally, we note that the phonon coupling to other degrees of freedom has been observed in nanomagnets [25], Gd [19] and other magnetic systems [14, 23, 24, 27, 57]. Shin *et al.* [58] showed even a quasi-static strain plays an important role in ultrafast spin dynamics. Rongione *et al.* [59] detected a bipolar strain wave-induced THz torque in the (001) oriented NiO/Pt film where the stress from the Pt layer launches the strain wave. Recently, Mashkovich *et al.* [60] employed the strong spin-lattice coupling in antiferromagnetic CoF₂ to excite phonons via magnons. For the same CoF₂ system, Disa *et al.* [61] did the opposite. They excited two degenerate E_u IR modes to displace the lattice along the optically inaccessible B_{2g} Raman mode, which transiently breaks the site symmetry between two Co atoms. The spin moments on two Co atoms do not compensate each other, and CoF₂ temporarily transitions to a ferrimagnet, with a net spin moment of $0.21 \mu_B$. The spin-phonon dispersion introduced here is expected to capture many opportunities in the entire Brillouin zone. This points out a new direction – the spin-phonon dispersion in excited states. Excited states often accommodate strong THz anharmonicity, leading to anharmonic frequency shifts through multiple phonon scattering.

V. CONCLUSIONS

We have introduced a much needed concept of the spin-phonon dispersion, where the second-derivative of the spin moment change is dispersed along the phonon crystal momentum. Our spin-phonon dispersion, with spin and phonon information both present, captures the complexity of the dependence of spin on the phonon, which goes beyond the spin-phonon coupling constant. The spin-phonon dispersion in hcp Co shows that a large portion of the Brillouin zone accommodates both spin reduction and increase, but this is not the case for bcc Fe. We only find a small pocket around the N point in bcc Fe that has spin moment reduction. This may help us understand the higher Curie temperature in Fe. Microscopically, we also understand why the spin-phonon dispersion has negative eigenvalues. In contrast to the vibrational force matrix, the off-diagonal matrix elements in the spin force matrix are larger than its diagonal counterparts, so the spin dynamical matrix contains the negative

eigenvalues. Our spin-phonon dispersion is also different from the magnon-phonon coupling [21] where the spin orientation, not the spin magnitude, is taken into account. Finally, our approach can be easily extended to systems where spin-orbit coupling should be taken into account. Thus, the spin-phonon dispersion represents an important paradigm shift and will have a significant impact on future research in both simple and complex quantum magnetic materials in spatial and time domains [49].

Acknowledgments

We acknowledge the helpful comments on our paper from Dr. Qihang Liu (SUST, China). MG was supported by Foundation for Distinguished Young Talents in Higher Education of Guangdong under Grant No. 2020KQNCX064, Shenzhen Science and Technology Innovation Council under Grant No. JCYJ20210324104812034, and Natural Science Foundation of Guangdong Province under Grant No. 2021A1515110389. GPZ and YHB were supported by the U.S. Department of Energy under Contract No. DE-FG02-06ER46304. Part of the work was done on Indiana State University's quantum and obsidian clusters. The research used resources of the National Energy Research Scientific Computing Center, which is supported by the Office of Science of the U.S. Department of Energy under Contract No. DE-AC02-05CH11231.

*guo-ping.zhang@outlook.com <https://orcid.org/0000-0002-1792-2701>

-
- [1] M. Kim, X. M. Chen, Y. I. Joe, E. Fradkin, P. Abbamonte, and S. L. Cooper, Mapping the Magnetostructural Quantum Phases of Mn_3O_4 , *Phys. Rev. Lett.* **104**, 136402 (2010).
 - [2] D. Zahn, F. Jakobs, Y. W. Windsor, H. Seiler, T. Vasileiadis, T. A. Butcher, Y. Qi, D. Engel, U. Atxitia, J. Vorberger, and R. Ernstorfer, Lattice dynamics and ultrafast energy flow between electrons, spins, and phonons in a 3d ferromagnet, *Phys. Rev. Research* **3**, 023032 (2021).
 - [3] G. P. Zhang, Y. H. Bai, and T. F. George, Optically and thermally driven huge lattice orbital and spin angular momenta from spinning fullerenes, *Phys. Rev. B* **104**, L100302 (2021).
 - [4] E. Anastassakis, E. Burstein, A. A. Maradudin and R. Minnick, Morphic effects. IV. Effects

- of an applied magnetic field on first-order photon-optical phonon interactions in non-magnetic crystals. *J. Phys. Chem. Solids* **33**, 1091 (1972).
- [5] R. Tackett, G. Lawes, B. C. Melot, M. Grossman, E. S. Toberer, and R. Seshadri, Magnetodielectric coupling in Mn_3O_4 , *Phys. Rev. B* **76**, 024409 (2007).
- [6] S. Hirai, A. M. dos Santos, M. C. Shapiro, J. J. Molaison, N. Pradhan, M. Guthrie, C. A. Tulk, I. R. Fisher, and W. L. Mao, Giant atomic displacement at a magnetic phase transition in metastable Mn_3O_4 , *Phys. Rev. B* **87**, 014417 (2013).
- [7] M. C. Kemei, J. K. Harada, R. Seshadri, and M. R. Suchomel, Structural change and phase coexistence upon magnetic ordering in the magnetodielectric spinel Mn_3O_4 , *Phys. Rev. B* **90**, 064418 (2014).
- [8] S. S. Hong, M. Gu, M. Verma, V. Harbola, B. Y. Wang, D. Lu, A. Vailionis, Y. Hikita, R. Pentcheva, J. M. Rondinelli and H. Y. Hwang, Extreme tensile strain states in $\text{La}_{0.7}\text{Ca}_{0.3}\text{MnO}_3$ membranes, *Science* **368**, 71 (2021).
- [9] T. Byrum, S. L. Gleason, A. Thaler, G. J. MacDougall, and S. L. Cooper, Effects of magnetic field and twin domains on magnetostructural phase mixture in Mn_3O_4 : Raman scattering studies of untwinned crystals, *Phys. Rev. B* **93**, 184418 (2016).
- [10] B. Wolin, X. Wang, T. Naibert, S. L. Gleason, G. J. MacDougall, H. D. Zhou, S. L. Cooper, and R. Budakian, Real-space magnetic imaging of the multiferroic spinels MnV_2O_4 and Mn_3O_4 , *Phys. Rev. Mater.* **2**, 064407 (2018).
- [11] P.-W. Ma, C. H. Woo, and S. L. Dudarev, Large-scale simulation of the spin-lattice dynamics in ferromagnetic iron, *Phys. Rev. B* **78**, 024434 (2008).
- [12] R. Lizarraga, F. Pan, L. Bergqvist, E. Holmström, Z. Gercsi, and L. Vitos, First-principles theory of the hcp-fcc phase transition in cobalt, *Sci. Rep.* **7**, 3778 (2017).
- [13] F.-G. Kuang, X.-Y. Kuang, S.-Y. Kang, and A.-J. Mao, Magneto-elastic effects and thermodynamic properties of ferromagnetic hcp Co, *Physica B: Condens. Matter* **441**, 72 (2014).
- [14] M. J. Verstraete, Ab initio calculation of spin-dependent electron-phonon coupling in iron and cobalt, *J. Phys.: Condens. Matter* **25**, 136001 (2013).
- [15] G. Lefkidis and W. Hübner, Ultrafast laser-driven magnetic-switching scenario in NiO: Role of phonons, *J. Magn. Magn. Mater.* **321**, 979 (2009).
- [16] S. Essert and H. C. Schneider, Electron-phonon scattering dynamics in ferromagnetic metals and their influence on ultrafast demagnetization processes, *Phys. Rev. B* **84**, 224405 (2011).

- [17] A. Baral, S. Vollmar, and H. C. Schneider, Magnetization dynamics and damping due to electron-phonon scattering in a ferrimagnetic exchange model, *Phys. Rev. B* **90**, 014427 (2014).
- [18] A. Melnikov, I. Radu, U. Bovensiepen, O. Krupin, K. Starke, E. Matthias, and M. Wolf, Coherent optical phonons and parametrically coupled magnons induced by femtosecond laser excitation of the Gd(0001) surface, *Phys. Rev. Lett.* **91**, 227403 (2003).
- [19] M. Sultan, U. Atxitia, A. Melnikov, O. Chubykalo-Fesenko, and U. Bovensiepen, Electron- and phonon-mediated ultrafast magnetization dynamics of Gd(0001), *Phys. Rev. B* **85**, 184407 (2012).
- [20] T. Henighan, M. Trigo, S. Bonetti, P. Granitzka, D. Higley, Z. Chen, M. P. Jiang, R. Kukreja, A. Gray, A. H. Reid, E. Jal, M. C. Hoffmann, M. Kozina, S. Song, M. Chollet, D. Zhu, P. F. Xu, J. Jeong, K. Carva, P. Maldonado, P. M. Oppeneer, M. G. Samant, S. S. P. Parkin, D. A. Reis, and H. A. Dürr, Generation mechanism of terahertz coherent acoustic phonons in Fe, *Phys. Rev. B* **93**, 220301(R) (2016).
- [21] R. Weber, Magnon-phonon coupling in metallic films, *Phys. Rev.* **169**, 451 (1968).
- [22] S. C. Guerkeiro and S. M. Kezende, *Rev. Brasileira Fisica* **1**, 207 (1971).
- [23] T.-M. Cheng and L. Li, Magnon-phonon coupling in two-dimensional Heisenberg ferromagnetic system, *J. Mag. Mag. Mater.* **320**, 1 (2008).
- [24] I. F. I. Mikhail, I. M. M. Ismail, and M. Ameen, Exact and model operators for magnon-phonon interactions in antiferromagnets, *Physica B: Condens. Matter* **406**, 508 (2011).
- [25] C. Berk, M. Jaris, W. Yang, S. Dhuey, S. Cabrini, and H. Schmidt, Strongly coupled magnon-phonon dynamics in a single nanomagnet, *Nat. Commun.* **10**, 2652 (2019).
- [26] T. J. Sjöstrand and F. Aryasetiawan, Magnon-phonon coupling from a crossing symmetric screened interaction, arXiv:2111.00908 (2021).
- [27] Y. Li, C. Zhao, W. Zhang, A. Hoffmann, and V. Novosad, Advances in coherent coupling between magnons and acoustic phonons, *APL Mater.* **9**, 060902 (2021).
- [28] D. Vaclavkova, M. Palit, J. Wyzula, S. Ghosh, A. Delhomme, S. Maity, P. Kapuscinski, A. Ghosh, M. Veis, M. Grzeszczyk, C. Faugeras, M. Orlita, S. Datta, and M. Potemski, Magnon polarons in the van der Waals antiferromagnet FePS₃, *Phys. Rev. B* **104**, 134437 (2021).
- [29] N. Pattanayak, J. Kumar, P. P. Patra, G. V. P. Kumar, and A. Bajpai, Signatures of spin-phonon coupling in hematite crystallites through dielectric and Raman spectroscopy, *EPL*

- 134**, 47003 (2021).
- [30] E. J. Elliot, Theory of the effect of spin-orbit coupling on magnetic resonance in some semiconductors, *Phys. Rev.* **96**, 266 (1954).
- [31] Y. Yafet, g Factors and spin-lattice relaxation of conduction electrons, *Solid State Phys.* **14**, 1 (1963).
- [32] J. Fabian and S. Das Sarma, Spin relaxation of conduction electrons in polyvalent metals: Theory and a realistic calculation, *Phys. Rev. Lett* **81**, 5624 (1998).
- [33] J. Fabian and S. Das Sarma, Phonon-induced spin relaxation of conduction electrons in aluminum, *Phys. Rev. Lett.* **83**, 1211 (1999).
- [34] M. S. Si and G. P. Zhang, Hot spin spots in the laser-induced demagnetization, *AIP Advances* **2**, 012158 (2012).
- [35] P. Blaha, K. Schwarz, G. K. H. Madsen, D. Kvasnicka, and J. Luitz, WIEN2k, An Augmented Plane Wave + Local Orbitals Program for Calculating Crystal Properties (Karlheinz Schwarz, Techn. Universität Wien, Austria, 2001).
- [36] G. Kresse and J. Furthmüller, *Comput. Mater. Sci.* **6**, 15 (1996).
- [37] G. P. Zhang, W. Hübner, G. Lefkidis, Y. Bai, and T. F. George, Paradigm of the time-resolved magneto-optical Kerr effect for femtosecond magnetism, *Nat. Phys.* **5**, 499 (2009).
- [38] M. Gu, Q. Xie, X. Shen, R. Xie, J. Wang, G. Tang, D. Wu, G. P. Zhang, and X. S. Wu, Magnetic Ordering and Structural Phase Transitions in a Strained Ultrathin SrRuO₃/SrTiO₃ Superlattice, *Phys. Rev. Lett.* **109**, 157003 (2012).
- [39] M. Gu, J. Wang, X. Wu, and G. P. Zhang, Stabilities of the intrinsic defects on SrTiO₃ surface and SrTiO₃/LaAlO₃ interface, *J. Phys. Chem. C* **116**, 24993 (2012).
- [40] G. P. Zhang, Y. H. Bai, and T. F. George, Ultrafast reduction of exchange splitting in ferromagnetic nickel, *J. Phys.: Condens. Matter* **28**, 236004 (2016).
- [41] G. P. Zhang, T. Jenkins, M. Bennett, and Y. H. Bai, Manifestation of intra-atomic 5d_{6s}-4f exchange coupling in photoexcited gadolinium, *J. Phys.: Condens. Matter* **29**, 495807 (2017).
- [42] R. Decker, A. Born, K. Ruotsalainen, K. Bauer, R. Haverkamp, R. Büchner, A. Pietzsch, and A. Föhlisch, Spin-lattice angular momentum transfer of localized and valence electrons in the demagnetization transient state of gadolinium, *Appl. Phys. Lett.* **119**, 152403 (2021).
- [43] B. Andres, S. E. Lee, and M. Weinelt, The role of spin-lattice coupling for ultrafast changes of the magnetic order in rare earth metals, arXiv:2108.04380v2, (2021).

- [44] G. P. Zhang, M. Gu, M. S. Si, T. F. George, and X. Wu, Current understanding of the laser-induced ultrafast (de)magnetization process, *Bul. Am. Phys. Soc.* **58**, W16.00011 (2013).
- [45] G. P. Zhang, M. Gu, Y. H. Bai, T. L. Jenkins, and T. F. George, Correlation between spin and orbital dynamics during laser-induced femtosecond demagnetization, *J. Phys. Chem. C* **125**, 14461 (2021).
- [46] G. P. Purja Pun and Y. Mishin, Embedded-atom potential for hcp and fcc cobalt, *Phys. Rev. B* **86**, 134116 (2012).
- [47] N. Wakabayashi, R. H. Scherm, and H. G. Smith, Lattice dynamics of Ti, Co, Tc, and other hcp transition metals, *Phys. Rev. B* **25**, 5122 (1982).
- [48] J. D. Watts, J. T. Batley, N. A. Rabideau, J. P. Hoch, L. O'Brien, P. A. Crowell, and C. Leighton. Finite-Size Effect in Phonon-Induced Elliott-Yafet Spin Relaxation in Al, *Phys. Rev. Lett.* **128**, 207201 (2022).
- [49] E. Beaurepaire, J. C. Merle, A. Daunois, and J.-Y. Bigot, Ultrafast spin dynamics in ferromagnetic nickel, *Phys. Rev. Lett.* **76**, 4250 (1996).
- [50] G. P. Zhang, W. Hübner, E. Beaurepaire, and J.-Y. Bigot, Laser-induced ultrafast demagnetization: Femtomagnetism, A new frontier? *Topics Appl. Phys.* **83**, 245 (2002).
- [51] A. Kirilyuk, A. V. Kimel, and Th. Rasing, Ultrafast optical manipulation of magnetic order, *Rev. Mod. Phys.* **82**, 2731 (2010). Erratum: *Rev. Mod. Phys.* **88**, 039904 (2016).
- [52] C. Dornes *et al.*, The ultrafast Einstein-de Haas effect, *Nature* **565**, 209 (2019).
- [53] S. R. Tauchert, M. Volkov, D. Ehberger, D. Kazenwadel, M. Evers, H. Lange, A. Donges, A. Book, W. Kreuzpaintner, U. Nowak and P. Baum, Polarized phonons carry angular momentum in ultrafast demagnetization, *Nature* **602**, 73 (2022).
- [54] T. Feng, X. Yang, and X. Ruan, Phonon anharmonic frequency shift induced by four-phonon scattering calculated from first principles, *J. Appl. Phys.* —bf 124, 145101 (2018).
- [55] M. Takahashi, M. Kowada, H. Matsui, E. Kwon, and Y. Ikemoto, Terahertz frequency shifts due to multiphonon scattering in thiamin crystals containing hydrated ions, *Appl. Phys. Lett.* **120**, 051104 (2022).
- [56] H. A. Mook, Magnetic moment distribution of nickel metal, *Phys. Rev.* **148**, 495 (1966).
- [57] S. Raut, S. Chakravarty, H. S. Mohanty, S. Mahapatra, S. Bhardwaj, A. M. Awasthi, B. Kar, K. Singh, M. Chandra, A. Lakhani, V. Ganesan, M. M. Patidar, R. K. Sharma, V. Srihari, H. K. Poswal, S. Mukherjee, S. Giri, and S. Panigrahi, Unveiling spinglass-like phase transition,

TABLE I: Spin ($\alpha, \beta, \gamma, \delta, \epsilon$) and phonon (a, b, g, d, e) parameters used for bcc Fe to compute the spin-phonon and phonon spectra, respectively, with $\alpha, \beta, \gamma, \delta, \epsilon$ in the units of $\mu_B/\text{\AA}^2$.

α	β	γ	δ	ϵ
1.4232	2.0323	4.4081	0.1126	1.0594
a	b	g	d	e
2.3876	1.736	11.7342	0.1163	1.9512

anisotropic negative thermal expansion and spin-phonon coupling induced ferroelectricity and magnetoelectric effect in polycrystalline $\text{Sm}_{0.5}\text{Y}_{0.5}\text{Fe}_{0.58}\text{Mn}_{0.42}\text{O}_3$, arXiv:2205.05291 (2022).

- [58] Y. Shin, M. Vomir, D.-H. Kim, P. C. Van, J.-R. Jeong, and J.-W. Kim, Quasi-static strain governing ultrafast spin dynamics, arXiv:2105.04168v1 (2021).
- [59] E. Rongione, O. Gueckstock, M. Mattern, O. Gomonay, H. Meer, C. Schmitt, R. Ramos, E. Saitoh, J. Sinova, H. Jaffres, M. Micica, J. Mangeney, S. T. B. Goennenwein, S. Geprags, T. Kampfrath, M. Kläui, M. Bargheer, T. S. Seifert, S. Dhillon, and R. Lebrun, Emission of coherent THz magnons in an antiferromagnetic insulator triggered by ultrafast spin-phonon interactions, arXiv:2205.11965 (2022).
- [60] E. A. Mashkovich, K. A. Grishunin, R. M. Dubrovin, A. K. Zvezdin, R. V. Pisarev, and A. V. Kimel, Terahertz-Light Driven Coupling of Antiferromagnetic Spins to Lattice, *Science* **374**, 1608 (2021).
- [61] A. S. Disa, M. Fechner, T. F. Nova, B. Liu, M. Först, D. Prabhakaran, P. G. Radaelli, and A. Cavalleri, Polarizing an antiferromagnet by optical engineering of the crystal field, *Nat. Phys.* **16**, 937 (2020).

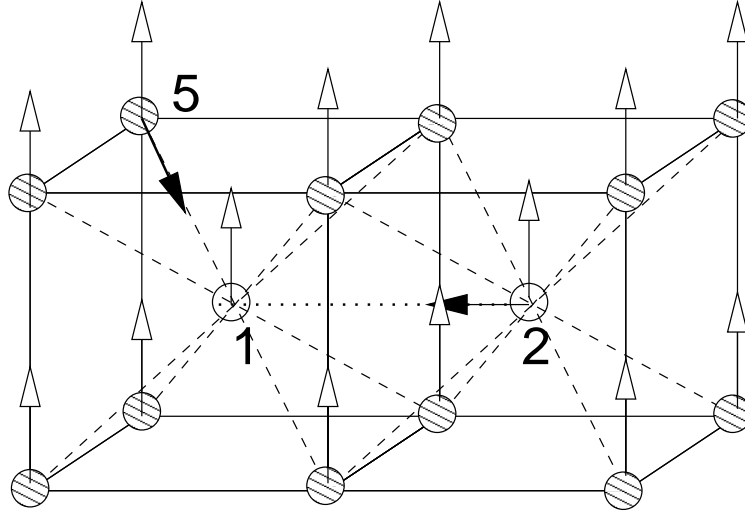


FIG. 1: An example of the two-cell bcc structure to explain how we compute the spin-phonon dispersion. Each atom's spin (empty arrows) is initialized along the z axis. The reference atom 1 is at the body center, with the eight first neighboring atoms denoted (shaded spheres), where atom 5 is just an example. The reference atom has six second-neighbor atoms, where atom 2 is just an example. For both bcc Fe and hcp Co, we adopt a $2 \times 2 \times 2$ supercell. The figure here is just a part of it, without an overly cumbersome diagram. Both the vibrational force and spin force matrices are computed by displacing one atom at one time. Two filled arrows denote two unique displacement directions.

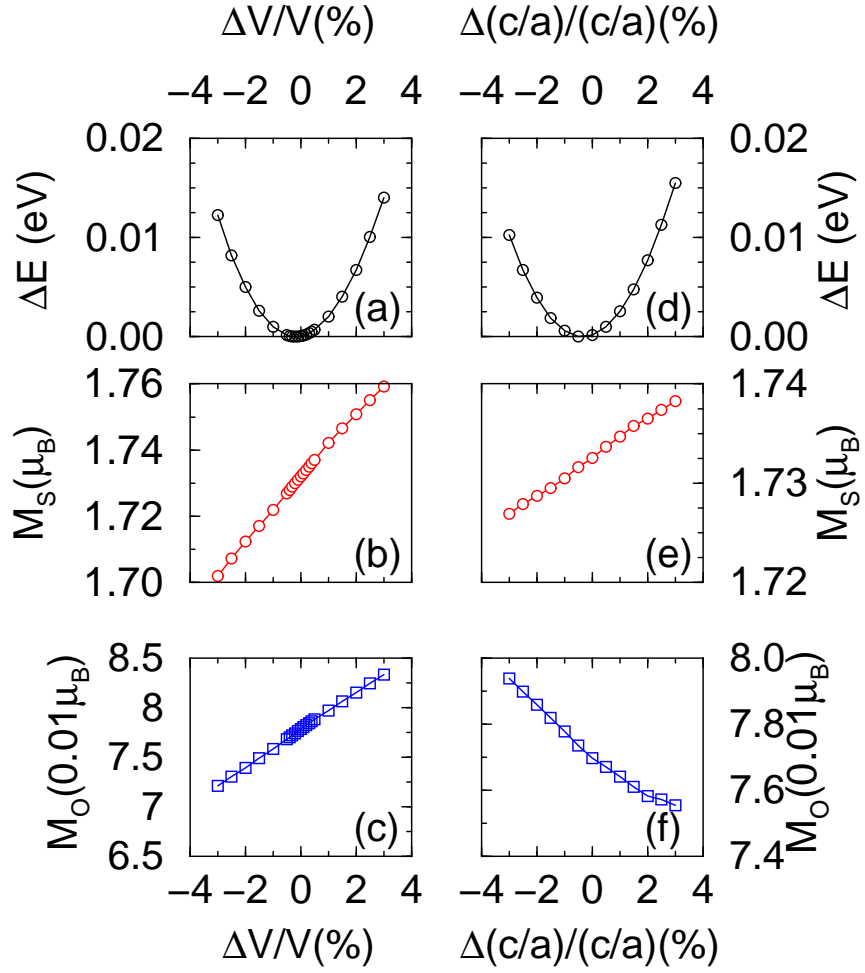


FIG. 2: (a) Total energy change ΔE as a function of $\Delta V/V$ for the breathing mode. ΔE is referenced with respect to the lowest total energy. The \mathbf{k} mesh is $33 \times 33 \times 17$. (b) and (c) are the spin and orbital moment changes as a function of $\Delta V/V$, respectively. (d) Total energy change ΔE for the stretching mode. The \mathbf{k} mesh is much larger, $53 \times 53 \times 28$. (e) and (f) are the spin and orbital moment changes as a function of $\Delta(c/a)/(c/a)$, respectively.

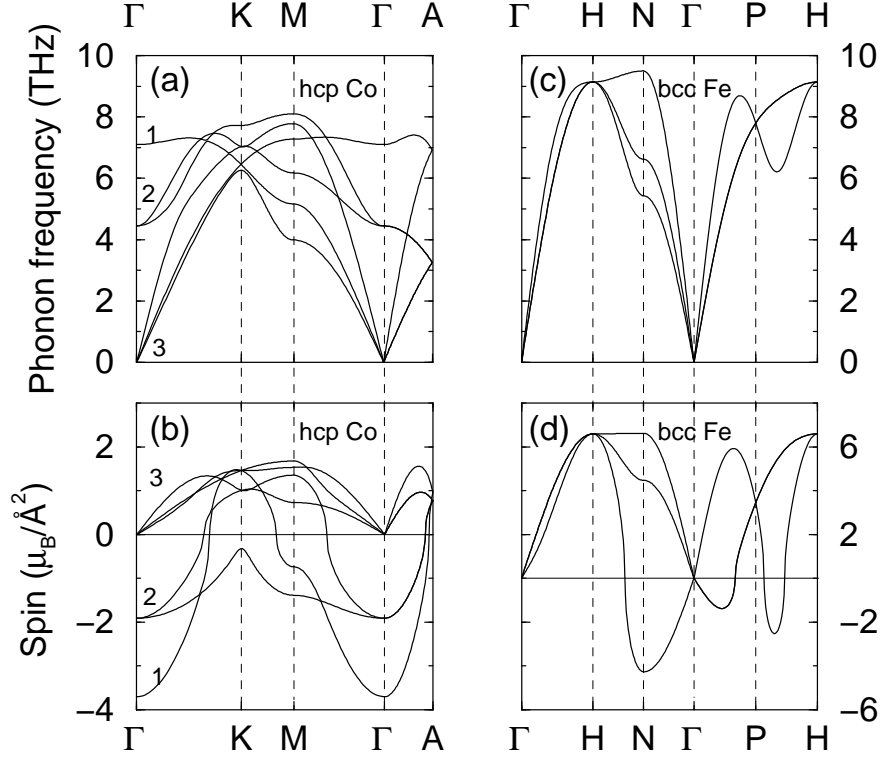


FIG. 3: (a) Phonon spectrum of hcp Co. (b) Spin-phonon dispersion for hcp Co. The total spin moment is expanded up to the second order. Both the positive and negative spin moment changes are noticed. Numbers around the Γ point in (a) and (b) denote the degeneracy of the bands. (c) Phonon spectrum of bcc Fe. (d) Spin-phonon dispersion for bcc Fe.

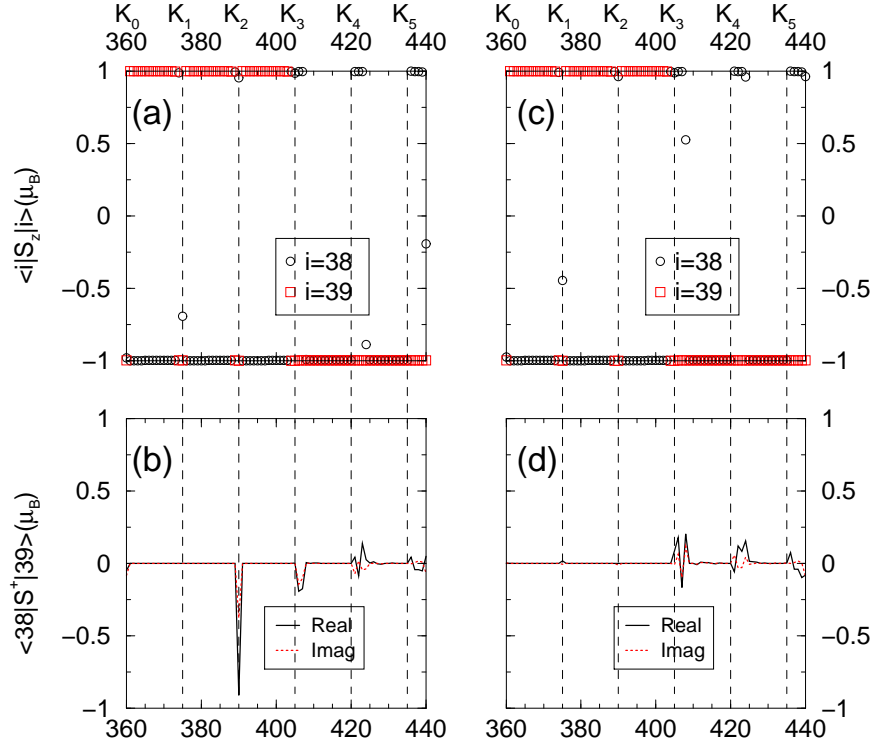


FIG. 4: (a) Spin expectation values of states $i = 38$ (circles) and $i = 39$ (boxes) along the crystal momentum for five segments with k_1 through k_5 , whose coordinates are given in the main text. The vertical dashed lines denote their locations. The numbers on the x axis are the k index of the k list, with the k mesh ($53 \times 53 \times 28$). (b) Spin flip matrix element $s^+ \langle 38|s^+|39\rangle$ between states 38 and 39. The element for s^- is tiny, not shown. The solid and dashed lines denote the real and imaginary parts, respectively. (c) and (d) are the same as (a) and (b), but for the distorted structure, with -0.5% contraction as Figs. 2(d), (e) and (f). This mimics the temperature effect. (c) shows the spin change is concentrated in some hot spin spots. (d) shows a larger spin flip change due to the lattice distortion. Even the location of the larger spin flip is changed. The largest change is now at k_3 .